Spectra and ratios of identified particles in Au + Au and d + Au collisions at $\sqrt{s_{NN}} = 200$ GeV

A. Adare,[13] S. Afanasiev,[30] C. Aidala,[43,44] N. N. Ajitanand,[62] Y. Akiba,[56,57] H. Al-Bataineh,[50] J. Alexander,[62] A. Angerami,[14] K. Aoki,[35,56] N. Apadula,[63] Y. Aramaki,[12,56] E. T. Atomssa,[36] R. Averbeck,[63] T. C. Awes,[52] B. Azmoun,[7] V. Babintsev,[24] M. Bai,[6] G. Baksay,[20] L. Baksay,[20] K. N. Barish,[8] B. Bassalleck,[49] A. T. Basye,[1] S. Bathe,[5,8,57] V. Baublis,[55] C. Baumann,[45] A. Bazilevsky,[7] S. Belikov,[7,*] R. Belmont,[44,67] R. Bennett,[63] A. Berdnikov,[59] Y. Berdnikov,[59] J. H. Bhom,[71] A. A. Bickley,[13] D. S. Blau,[34] J. S. Bok,[71] K. Boyle,[63] M. L. Brooks,[39] H. Buesching,[7] V. Bumazhnov,[24] G. Bunce,[7,57] S. Butsyk,[39] C. M. Camacho,[39] S. Campbell,[63] A. Caringi,[46] C.-H. Chen,[63] C. Y. Chi,[14] M. Chiu,[7] I. J. Choi,[71] J. B. Choi,[10] R. K. Choudhury,[4] P. Christiansen,[41] T. Chujo,[66] P. Chung,[62] O. Chvala,[8] V. Cianciolo,[52] Z. Citron,[63] B. A. Cole,[14] Z. Conesa del Valle,[36] M. Connors,[63] P. Constantin,[39] M. Csanád,[18] T. Csörgő,[70] T. Dahms,[63] S. Dairaku,[35,56] I. Danchev,[67] K. Das,[21] A. Datta,[43] G. David,[7] M. K. Dayananda,[22] A. Denisov,[24] A. Deshpande,[57,63] E. J. Desmond,[7] K. V. Dharmawardane,[50] O. Dietzsch,[60] A. Dion,[28,63] M. Donadelli,[60] O. Drapier,[36] A. Drees,[63] K. A. Drees,[6] J. M. Durham,[39,63] A. Durum,[24] D. Dutta,[4] L. D'Orazio,[42] S. Edwards,[21] Y. V. Efremenko,[52] F. Ellinghaus,[13] T. Engelmore,[14] A. Enokizono,[38,52] H. En'yo,[56,57] S. Esumi,[66] B. Fadem,[46] D. E. Fields,[49] M. Finger,[9] M. Finger, Jr.,[9] F. Fleuret,[36] S. L. Fokin,[34] Z. Fraenkel,[69,*] J. E. Frantz,[51,63] A. Franz,[7] A. D. Frawley,[21] K. Fujiwara,[56] Y. Fukao,[56] T. Fusayasu,[48] I. Garishvili,[64] A. Glenn,[13,38] H. Gong,[63] M. Gonin,[36] Y. Goto,[56,57] R. Granier de Cassagnac,[36] N. Grau,[2,14] S. V. Greene,[67] G. Grim,[39] M. Grosse Perdekamp,[25,57] T. Gunji,[12] H.-Å. Gustafsson,[41,*] J. S. Haggerty,[7] K. I. Hahn,[19] H. Hamagaki,[12] J. Hamblen,[64] R. Han,[54] J. Hanks,[14] E. P. Hartouni,[38] E. Haslum,[41] R. Hayano,[12] X. He,[22] M. Heffner,[38] T. K. Hemmick,[63] T. Hester,[8] J. C. Hill,[28] M. Hohlmann,[20] W. Holzmann,[14] K. Homma,[23] B. Hong,[33] T. Horaguchi,[23] D. Hornback,[64] S. Huang,[67] T. Ichihara,[56,57] R. Ichimiya,[56] J. Ide,[46] Y. Ikeda,[66] K. Imai,[29,35,56] M. Inaba,[66] D. Isenhower,[1] M. Ishihara,[56] T. Isobe,[12,56] M. Issah,[67] A. Isupov,[30] D. Ivanischev,[55] Y. Iwanaga,[23] B. V. Jacak,[63] J. Jia,[7,62] X. Jiang,[39] J. Jin,[14] B. M. Johnson,[7] T. Jones,[1] K. S. Joo,[47] D. Jouan,[53] D. S. Jumper,[1] F. Kajihara,[12] S. Kametani,[56] N. Kamihara,[57] J. Kamin,[63] J. H. Kang,[71] J. Kapustinsky,[39] K. Karatsu,[35,56] M. Kasai,[56,58] D. Kawall,[43,57] M. Kawashima,[56,58] A. V. Kazantsev,[34] T. Kempel,[28] A. Khanzadeev,[55] K. M. Kijima,[23] J. Kikuchi,[68] A. Kim,[19] B. I. Kim,[33] D. H. Kim,[47] D. J. Kim,[31] E. Kim,[61] E.-J. Kim,[10] S. H. Kim,[71] Y.-J. Kim,[25] E. Kinney,[13] K. Kiriluk,[13] Á. Kiss,[18] E. Kistenev,[7] D. Kleinjan,[8] L. Kochenda,[55] B. Komkov,[55] M. Konno,[66] J. Koster,[25] D. Kotchetkov,[49] A. Kozlov,[69] A. Král,[15] A. Kravitz,[14] G. J. Kunde,[39] K. Kurita,[56,58] M. Kurosawa,[56] Y. Kwon,[71] G. S. Kyle,[50] R. Lacey,[62] Y. S. Lai,[14] J. G. Lajoie,[28] A. Lebedev,[28] D. M. Lee,[39] J. Lee,[19] K. Lee,[61] K. B. Lee,[33] K. S. Lee,[33] M. J. Leitch,[39] M. A. L. Leite,[60] E. Leitner,[67] B. Lenzi,[60] X. Li,[11] P. Lichtenwalner,[46] P. Liebing,[57] L. A. Linden Levy,[13] T. Liška,[15] A. Litvinenko,[30] H. Liu,[39,50] M. X. Liu,[39] B. Love,[67] R. Luechtenborg,[45] D. Lynch,[7] C. F. Maguire,[67] Y. I. Makdisi,[6] A. Malakhov,[30] M. D. Malik,[49] V. I. Manko,[34] E. Mannel,[14] Y. Mao,[54,56] H. Masui,[66] F. Matathias,[14] M. McCumber,[63] P. L. McGaughey,[39] D. McGlinchey,[13,21] N. Means,[63] B. Meredith,[25] Y. Miake,[66] T. Mibe,[32] A. C. Mignerey,[42] P. Mikeš,[9,27] K. Miki,[56,66] A. Milov,[7] M. Mishra,[3] J. T. Mitchell,[7] A. K. Mohanty,[4] H. J. Moon,[47] Y. Morino,[12] A. Morreale,[8] D. P. Morrison,[7,†] T. V. Moukhanova,[34] T. Murakami,[35] J. Murata,[56,58] S. Nagamiya,[32] J. L. Nagle,[13,‡] M. Naglis,[69] M. I. Nagy,[18,70] I. Nakagawa,[56,57] Y. Nakamiya,[23] K. R. Nakamura,[35,56] T. Nakamura,[23,32,56] K. Nakano,[56,65] S. Nam,[19] J. Newby,[38] M. Nguyen,[63] M. Nihashi,[23] R. Nouicer,[7] A. S. Nyanin,[34] C. Oakley,[22] E. O'Brien,[7] S. X. Oda,[12] C. A. Ogilvie,[28] M. Oka,[66] K. Okada,[57] Y. Onuki,[56] A. Oskarsson,[41] M. Ouchida,[23,56] K. Ozawa,[12] R. Pak,[7] V. Pantuev,[26,63] V. Papavassiliou,[50] I. H. Park,[19] J. Park,[61] S. K. Park,[33] W. J. Park,[33] S. F. Pate,[50] H. Pei,[28] J.-C. Peng,[25] H. Pereira,[16] V. Peresedov,[30] D. Yu. Peressounko,[34] R. Petti,[63] C. Pinkenburg,[7] R. P. Pisani,[7] M. Proissl,[63] M. L. Purschke,[7] A. K. Purwar,[39] H. Qu,[22] J. Rak,[31] A. Rakotozafindrabe,[36] I. Ravinovich,[69] K. F. Read,[52,64] S. Rembeczki,[20] K. Reygers,[45] V. Riabov,[55] Y. Riabov,[55] E. Richardson,[42] D. Roach,[67] G. Roche,[40] S. D. Rolnick,[8] M. Rosati,[28] C. A. Rosen,[13] S. S. E. Rosendahl,[41] P. Rosnet,[40] P. Rukoyatkin,[30] P. Ružička,[27] B. Sahlmueller,[45,63] N. Saito,[32] T. Sakaguchi,[7] K. Sakashita,[56,65] V. Samsonov,[55] S. Sano,[12,68] T. Sato,[66] S. Sawada,[32] K. Sedgwick,[8] J. Seele,[13] R. Seidl,[25,57] A. Yu. Semenov,[28] R. Seto,[8] D. Sharma,[69] I. Shein,[24] T.-A. Shibata,[56,65] K. Shigaki,[23] M. Shimomura,[66] K. Shoji,[35,56] P. Shukla,[4] A. Sickles,[7] C. L. Silva,[28,60] D. Silvermyr,[52] C. Silvestre,[16] K. S. Sim,[33] B. K. Singh,[3] C. P. Singh,[3] V. Singh,[3] M. Slunečka,[9] R. A. Soltz,[38] W. E. Sondheim,[39] S. P. Sorensen,[64] I. V. Sourikova,[7] N. A. Sparks,[1] P. W. Stankus,[52] E. Stenlund,[41] S. P. Stoll,[7] T. Sugitate,[23] A. Sukhanov,[7] J. Sziklai,[70] E. M. Takagui,[60] A. Taketani,[56,57] R. Tanabe,[66] Y. Tanaka,[48] S. Taneja,[63] K. Tanida,[35,56,57] M. J. Tannenbaum,[7] S. Tarafdar,[3] A. Taranenko,[62] P. Tarján,[17] H. Themann,[63] D. Thomas,[1] T. L. Thomas,[49] M. Togawa,[35,56,57] A. Toia,[63] L. Tomášek,[27] H. Torii,[23] R. S. Towell,[1] I. Tserruya,[69] Y. Tsuchimoto,[23] C. Vale,[7,28] H. Valle,[67] H. W. van Hecke,[39] E. Vazquez-Zambrano,[14] A. Veicht,[25] J. Velkovska,[67] R. Vértesi,[17,70] A. A. Vinogradov,[34] M. Virius,[15] V. Vrba,[27] E. Vznuzdaev,[55] X. R. Wang,[50] D. Watanabe,[23] K. Watanabe,[66] Y. Watanabe,[56,57] F. Wei,[28] R. Wei,[62] J. Wessels,[45] S. N. White,[7] D. Winter,[14] J. P. Wood,[1] C. L. Woody,[7] R. M. Wright,[1] M. Wysocki,[13] W. Xie,[57] Y. L. Yamaguchi,[12] K. Yamaura,[23] R. Yang,[25] A. Yanovich,[24] J. Ying,[22] S. Yokkaichi,[56,57] Z. You,[54] G. R. Young,[52] I. Younus,[37,49] I. E. Yushmanov,[34] W. A. Zajc,[14] C. Zhang,[52] S. Zhou,[11] and L. Zolin[30]

(PHENIX Collaboration)

[1]*Abilene Christian University, Abilene, Texas 79699, USA*

[2]*Department of Physics, Augustana College, Sioux Falls, South Dakota 57197, USA*

[3]*Department of Physics, Banaras Hindu University, Varanasi 221005, India*

[4]*Bhabha Atomic Research Centre, Bombay 400 085, India*

[5]*Baruch College, City University of New York, New York, New York, 10010 USA*
[6]*Collider-Accelerator Department, Brookhaven National Laboratory, Upton, New York 11973-5000, USA*
[7]*Physics Department, Brookhaven National Laboratory, Upton, New York 11973-5000, USA*
[8]*University of California - Riverside, Riverside, California 92521, USA*
[9]*Charles University, Ovocný trh 5, Praha 1, 116 36, Prague, Czech Republic*
[10]*Chonbuk National University, Jeonju, 561-756, Korea*
[11]*Science and Technology on Nuclear Data Laboratory, China Institute of Atomic Energy, Beijing 102413, People's Republic of China*
[12]*Center for Nuclear Study, Graduate School of Science, University of Tokyo, 7-3-1 Hongo, Bunkyo, Tokyo 113-0033, Japan*
[13]*University of Colorado, Boulder, Colorado 80309, USA*
[14]*Columbia University, New York, New York 10027 and Nevis Laboratories, Irvington, New York 10533, USA*
[15]*Czech Technical University, Zikova 4, 166 36 Prague 6, Czech Republic*
[16]*Dapnia, CEA Saclay, F-91191 Gif-sur-Yvette, France*
[17]*Debrecen University, H-4010 Debrecen, Egyetem tér 1, Hungary*
[18]*ELTE, Eötvös Loránd University, H-1117 Budapest, Pázmány P.s. 1/A, Hungary*
[19]*Ewha Womans University, Seoul 120-750, Korea*
[20]*Florida Institute of Technology, Melbourne, Florida 32901, USA*
[21]*Florida State University, Tallahassee, Florida 32306, USA*
[22]*Georgia State University, Atlanta, Georgia 30303, USA*
[23]*Hiroshima University, Kagamiyama, Higashi-Hiroshima 739-8526, Japan*
[24]*IHEP Protvino, State Research Center of Russian Federation, Institute for High Energy Physics, Protvino 142281, Russia*
[25]*University of Illinois at Urbana-Champaign, Urbana, Illinois 61801, USA*
[26]*Institute for Nuclear Research of the Russian Academy of Sciences, prospekt 60-letiya Oktyabrya 7a, Moscow 117312, Russia*
[27]*Institute of Physics, Academy of Sciences of the Czech Republic, Na Slovance 2, 182 21 Prague 8, Czech Republic*
[28]*Iowa State University, Ames, Iowa 50011, USA*
[29]*Advanced Science Research Center, Japan Atomic Energy Agency, 2-4 Shirakata Shirane, Tokai-mura, Naka-gun, Ibaraki-ken 319-1195, Japan*
[30]*Joint Institute for Nuclear Research, 141980 Dubna, Moscow Region, Russia*
[31]*Helsinki Institute of Physics and University of Jyväskylä, P. O. Box 35, FI-40014 Jyväskylä, Finland*
[32]*KEK, High Energy Accelerator Research Organization, Tsukuba, Ibaraki 305-0801, Japan*
[33]*Korea University, Seoul 136-701, Korea*
[34]*Russian Research Center "Kurchatov Institute," Moscow 123098 Russia*
[35]*Kyoto University, Kyoto 606-8502, Japan*
[36]*Laboratoire Leprince-Ringuet, Ecole Polytechnique, CNRS-IN2P3, Route de Saclay, F-91128 Palaiseau, France*
[37]*Physics Department, Lahore University of Management Sciences, Lahore, Pakistan*
[38]*Lawrence Livermore National Laboratory, Livermore, California 94550, USA*
[39]*Los Alamos National Laboratory, Los Alamos, New Mexico 87545, USA*
[40]*LPC, Université Blaise Pascal, CNRS-IN2P3, Clermont-Fd, 63177 Aubiere Cedex, France*
[41]*Department of Physics, Lund University, Box 118, SE-221 00 Lund, Sweden*
[42]*University of Maryland, College Park, Maryland 20742, USA*
[43]*Department of Physics, University of Massachusetts, Amherst, Massachusetts 01003-9337, USA*
[44]*Department of Physics, University of Michigan, Ann Arbor, Michigan 48109-1040, USA*
[45]*Institut fur Kernphysik, University of Muenster, D-48149 Muenster, Germany*
[46]*Muhlenberg College, Allentown, Pennsylvania 18104-5586, USA*
[47]*Myongji University, Yongin, Kyonggido 449-728, Korea*
[48]*Nagasaki Institute of Applied Science, Nagasaki-shi, Nagasaki 851-0193, Japan*
[49]*University of New Mexico, Albuquerque, New Mexico 87131, USA*
[50]*New Mexico State University, Las Cruces, New Mexico 88003, USA*
[51]*Department of Physics and Astronomy, Ohio University, Athens, Ohio 45701, USA*
[52]*Oak Ridge National Laboratory, Oak Ridge, Tennessee 37831, USA*
[53]*IPN-Orsay, Universite Paris Sud, CNRS-IN2P3, BP1, F-91406, Orsay, France*
[54]*Peking University, Beijing 100871, People's Republic of China*
[55]*PNPI, Petersburg Nuclear Physics Institute, Gatchina, Leningrad Region 188300, Russia*
[56]*RIKEN Nishina Center for Accelerator-Based Science, Wako, Saitama 351-0198, Japan*
[57]*RIKEN BNL Research Center, Brookhaven National Laboratory, Upton, New York 11973-5000, USA*
[58]*Physics Department, Rikkyo University, 3-34-1 Nishi-Ikebukuro, Toshima, Tokyo 171-8501, Japan*
[59]*Saint Petersburg State Polytechnic University, St. Petersburg, 195251 Russia*
[60]*Universidade de São Paulo, Instituto de Física, Caixa Postal 66318, São Paulo CEP05315-970, Brazil*
[61]*Seoul National University, Seoul, Korea*

[62]*Chemistry Department, Stony Brook University, SUNY, Stony Brook, New York 11794-3400, USA*
[63]*Department of Physics and Astronomy, Stony Brook University, SUNY, Stony Brook, New York 11794-3400, USA*
[64]*University of Tennessee, Knoxville, Tennessee 37996, USA*
[65]*Department of Physics, Tokyo Institute of Technology, Oh-okayama, Meguro, Tokyo 152-8551, Japan*
[66]*Institute of Physics, University of Tsukuba, Tsukuba, Ibaraki 305, Japan*
[67]*Vanderbilt University, Nashville, Tennessee 37235, USA*
[68]*Waseda University, Advanced Research Institute for Science and Engineering, 17 Kikui-cho, Shinjuku-ku, Tokyo 162-0044, Japan*
[69]*Weizmann Institute, Rehovot 76100, Israel*
[70]*Institute for Particle and Nuclear Physics, Wigner Research Centre for Physics, Hungarian Academy of Sciences (Wigner RCP, RMKI) H-1525 Budapest 114, P. O. Box 49, Budapest, Hungary*
[71]*Yonsei University, IPAP, Seoul 120-749, Korea*
(Received 12 April 2013; published 22 August 2013)

The transverse momentum (p_T) spectra and ratios of identified charged hadrons ($\pi^{\pm}$, $K^{\pm}$, p, $\bar{p}$) produced in $\sqrt{s_{NN}} = 200$ GeV Au + Au and d + Au collisions are reported in five different centrality classes for each collision species. The measurements of pions and protons are reported up to $p_T = 6$ GeV/c (5 GeV/c), and the measurements of kaons are reported up to $p_T = 4$ GeV/c (3.5 GeV/c) in Au + Au (d + Au) collisions. In the intermediate p_T region, between 2 and 5 GeV/c, a significant enhancement of baryon-to-meson ratios compared to those measured in $p + p$ collisions is observed. This enhancement is present in both Au + Au and d + Au collisions and increases as the collisions become more central. We compare a class of peripheral Au + Au collisions with a class of central d + Au collisions which have a comparable number of participating nucleons and binary nucleon-nucleon collisions. The p_T-dependent particle ratios for these classes display a remarkable similarity, which is then discussed.

DOI: 10.1103/PhysRevC.88.024906 PACS number(s): 25.75.Dw, 25.75.Ld

I. INTRODUCTION

Measurements of identified particles in Au + Au collisions allow the study of particle-production mechanisms in a hot and dense nuclear medium and probe the properties of the quark-gluon plasma (QGP) [1–4]. In d + Au collisions, these measurements allow the study of cold-nuclear-matter effects on particle production, such as the Cronin enhancement [5,6], nuclear shadowing [7], and gluon saturation [8]. These cold-nuclear-matter effects are present in Au + Au collisions as well, and the study of d + Au collisions allows us to determine these effects directly and to disentangle them from the effects of the hot and dense nuclear medium.

One of the most intriguing discoveries in the early days of the research program at the Relativistic Heavy Ion Collider was the significantly enhanced baryon production relative to meson production at intermediate transverse momentum 2 GeV/c < p_T < 5 GeV/c, as evidenced in the large baryon-to-meson ratios and the significant differences in the particle suppression patterns measured by the nuclear modification factors [9–11]. Several classes of models were introduced to explain these differences based on different physical phenomena, such as strong radial flow [12,13], baryon junctions [14,15], and hadronization through recombination [16–21].

Additionally, the recombination model has been employed to explain the baryon vs meson difference in the Cronin enhancement observed in p + A collisions [22,23]. Traditional explanations of the Cronin enhancement involve the multiple soft scatterings in the initial state prior to the hard scattering and subsequent fragmentation of the hard scattered parton [24]. This process can naturally explain the deficit of particle production at low p_T and enhancement at intermediate p_T, but does not account for the particle species dependence at Relativistic Heavy Ion Collider energies [25]. Conversely, in the recombination model, the observed enhancement is attributed to final-state effects, i.e., the recombination of soft partons from the nuclear medium with hard scattered partons in a jet. For this reason d + Au collisions represent an excellent testing ground for the recombination model, because hot-nuclear-matter effects, such as the collective expansion of the medium, are not expected. However, recent results in d + Au collisions at 200 GeV [26] and p + Pb collisions at 5.02 TeV [27–29] suggest that some collective expansion effects may be present in the most central events.

Measurements of strange particles, such as charged kaons, have also been an interesting subject in heavy-ion collisions. An enhancement of strangeness production relative to that in $p + p$ collisions has been observed at various collision energies [30]. This strangeness enhancement is a possible signature of deconfinement, thermalization, and flavor equilibration [31,32]. In this scenario, strangeness production is dominated by thermal gluon fusion. The measurement of charged kaons in a broad p_T range and in different centrality classes is a significant tool to further understand the thermalization of the system and the mechanism of strangeness production.

To address the particle production in both hot and cold QCD matter, a systematic study of identified particles over a broad p_T range with a wide selection of centralities in both Au + Au and d + Au collisions is required. In this paper, the spectra, particle ratios, and nuclear modification factors previously reported by PHENIX in Au + Au [10] and d + Au collisions [25] are revisited, extending the p_T reach

*Deceased.
†PHENIX cospokesperson: morrison@bnl.gov
‡PHENIX cospokesperson: jamie.nagle@colorado.edu

of previous measurements and significantly improving the statistical precision. In Sec. II we discuss the experimental apparatus and the detector subsystems used in this analysis; in Sec. III we discuss the analysis method, including event and track selection, and particle identification; in Sec. IV we discuss the results; and in Sec. V we summarize our findings.

II. EXPERIMENTAL SETUP

The PHENIX experiment is a large, general-purpose detector with a wide variety of detector subsystems ideally suited to the study of nuclear matter in conditions of extreme temperature and density. PHENIX is composed of global event property detectors, forward and backward rapidity arms (North and South) dedicated to muon measurements, and two central arm spectrometers (East and West) at midrapidity covering pseudorapidity $|\eta| < 0.35$ for measurements of photons, electrons, and charged hadrons. Detailed descriptions of the various detector subsystems can be found in Ref. [33].

Figure 1 gives a schematic diagram of the PHENIX detector for the 2007 configuration; the 2008 configuration is very similar. The top panel shows the central spectrometer arms, viewed along the beamline, facing North. The bottom panel shows the two forward rapidity muon arms (North and South) and the global detectors.

The analysis presented herein makes use of the beam-beam counters, the tracking system (drift chamber and two layers of pad chambers), the electromagnetic calorimeter, and the time-of-flight detector in the West arm.

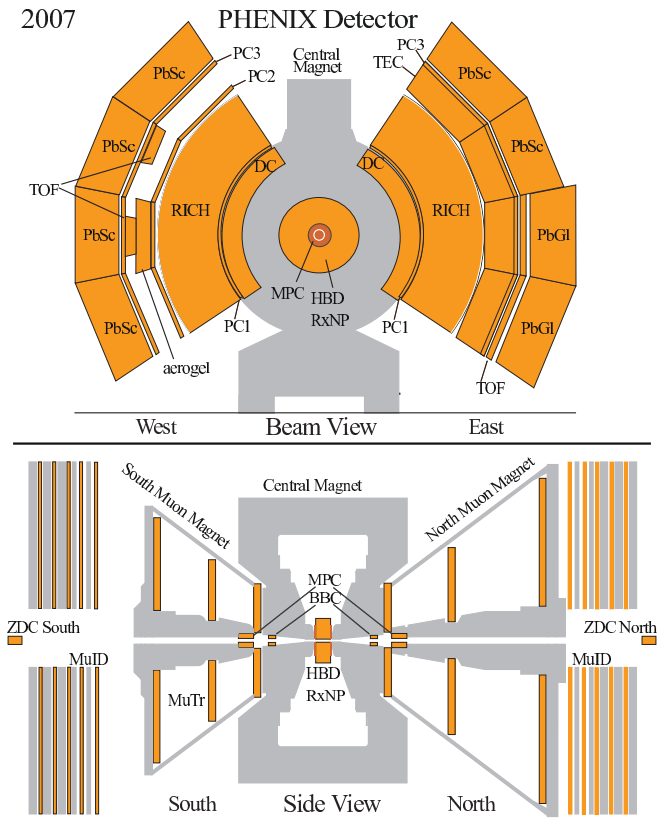

FIG. 1. (Color online) The PHENIX detector configuration for the 2007 data taking period. The 2008 configuration is very similar.

A. Detector subsystems

The beam-beam counters (BBCs) are used for the minimum-bias trigger, the centrality definition, the determination of the collision vertex along the beam axis (the z vertex), and the event start time. The BBCs [34,35] are located at ± 144 cm from the nominal interaction point. They cover 2π in azimuth and a pseudorapidity range of $3.0 < |\eta| < 3.9$. Each BBC is an array of 64 identical hexagonal detector elements, with the beam pipe passing through the center of the array. Each element is a quartz Čerenkov radiation counter, and the radiator and photomultiplier tube are constructed as a single piece.

The PHENIX tracking system is optimized for the high-multiplicity environment of ultrarelativistic heavy-ion collisions. It comprises drift chambers (DCs) [36] and pad chambers (PC1, PC2, and PC3) [37]. This analysis makes use of the first layer of pad chambers (PC1) and the third layer (PC3). The DCs have an active volume in the radial range $2.02 \text{ m} < r < 2.46$ m. The PC1 is mated directly to the back of the DC frame in each arm at a radial distance of 2.49 m. The PC3 is located in each arm at a radial distance of 4.98 m.

The primary particle identification detector used in this analysis is the time-of-flight detector in the West half of the central arm spectrometer (TOFW). The TOFW [38,39] is located at a radial distance of 4.81 m from the interaction point, having pseudorapidity coverage of $|\eta| < 0.35$ and azimuthal coverage of 22° in two separate sections. The individual elements are multigap resistive plate chambers (MRPCs). Each MRPC has six 230-μm gas gaps separated by five 550-μm-thick glass plates. On each side of the outermost glass plates (1.1 mm thick) are carbon-tape electrodes held at $+7$ kV on one side and -7 kV on the other side, for a total bias voltage of 14 kV. When charged particles traverse the detector, the gas between the plates is ionized and the image charge is collected at each side of the chamber on four copper readout strips. Each strip has dimensions of 37×2.8 cm with a separation of 0.3 cm. The strips are oriented lengthwise along the azimuthal direction. Each strip is read out from both top and bottom so that the time difference between them can be used to determine the hit position along the length of the strip with a resolution of order 1 cm. The TOFW system is composed of a total of 128 MRPCs, 512 strips, and 1024 readouts. The total timing resolution, which includes the uncertainty in the start time from the BBC, is 84 ps in Au + Au collisions [39]. In d + Au collisions it is 95 ps, where the slightly poorer resolution is attributable to the lower resolution of the start time determination from the BBC. This is attributable to the lower multiplicity in d + Au collisions and, for the same reason, the z-vertex resolution is also poorer in d + Au collisions.

III. ANALYSIS METHOD

A. Event and track selection

This paper presents an analysis of Au + Au collisions at $\sqrt{s_{NN}} = 200$ GeV, collected in 2007, and d + Au collisions at $\sqrt{s_{NN}} = 200$ GeV, collected in 2008. For each set we select events that pass the minimum-bias trigger, which is defined as a coincidence between the North and South BBCs. In Au + Au

TABLE I. Values of $\langle N_{\rm coll}\rangle$ and $\langle N_{\rm part}\rangle$ for Au + Au and d + Au collisions from Glauber model simulations.

Collision	Centrality (%)	$\langle N_{\rm coll}\rangle$	$\langle N_{\rm part}\rangle$
Au + Au	0–10	960.2 ± 96.1	325.8 ± 3.8
	10–20	609.5 ± 59.8	236.1 ± 5.5
	20–40	300.8 ± 29.6	141.5 ± 5.8
	40–60	94.2 ± 12.0	61.6 ± 5.1
	60–92	14.8 ± 3.0	14.7 ± 2.9
d + Au	0–20	15.1 ± 1.0	15.3 ± 0.8
	20–40	10.2 ± 0.7	11.1 ± 0.6
	40–60	6.6 ± 0.4	7.8 ± 0.4
	60–88	3.1 ± 0.2	4.3 ± 0.2
	0–100	7.6 ± 0.4	8.5 ± 0.4

collisions, this trigger requires two or more photomultiplier tubes firing in each BBC and measures 92 ± 3% of the total inelastic cross section; in d + Au collisions, it requires one or more photomultiplier tubes firing in each BBC and measures 88 ± 4% of the total inelastic cross section. We have an additional requirement that the collision vertex is within $|z| < 30$ cm of the nominal origin of the coordinate system.

Centrality selection is performed with the BBCs using the Glauber Monte Carlo procedure described in Ref. [40], in which the charge in each BBC detector is assumed to be proportional to the number of participating nucleons $N_{\rm part}$ traveling towards it. For the Au + Au system the North and South BBC distributions are summed, but for the d + Au system, only the South (Au-going) side is used. The BBC charge is assumed to follow a negative binomial distribution (NBD) with a mean of $N_{\rm part}$ and the remaining NBD parameters determined from a χ^2 minimization of the combined Glauber + NBD calculation with respect to the data. The BBC distributions are divided into equal probability bins, and the corresponding Glauber distributions are used to calculate $N_{\rm part}$ as well as the number of binary nucleon-nucleon collisions $N_{\rm coll}$, as shown in Table I. We also present the number of deuteron participants $N_{\rm part,d}$ and the number of Au participants $N_{\rm part,Au}$ in d + Au collisions in Table II.

Charged track reconstruction in the DC is based on a combinatorial Hough transform, which gives the angle in the main bend plane (r-ϕ) and thus p_T. The PC1 is used to determine the hit position in the longitudinal (z) direction. Only tracks with valid information in both the DC and the PC1 are used in this analysis. Tracks in DC/PC1 are projected to the outer detectors, such as PC3 and TOFW, and matched to hits in those detectors with the minimum distance between the projection and the hit position. The distribution of differences between hits and projections is approximately Gaussian, with an additional underlying background caused by random associations. Only tracks with a difference of less than two standard deviations in both the azimuthal and the longitudinal directions in both the PC3 and the TOFW are selected, so as to minimize background contamination. In the Au + Au data for $p_T > 5.0$ GeV/c, an additional background isolation cut is applied. For these tracks we require $E/p_T > 0.2$, where E is the energy deposited in the electromagnetic calorimeter. This cut removes low-p_T particles that are falsely reconstructed as high-p_T tracks.

TABLE II. Values of $\langle N_{{\rm part},d}\rangle$, $\langle N_{\rm part,Au}\rangle$, and $\langle N_{\rm part}\rangle$ for d + Au collisions from Glauber model simulations.

Centrality (%)	$\langle N_{{\rm part},d}\rangle$	$\langle N_{\rm part,Au}\rangle$	$\langle N_{\rm part}\rangle$
0–20	1.95 ± 0.01	13.33 ± 0.82	15.28 ± 0.83
20–40	1.84 ± 0.01	9.27 ± 0.63	11.11 ± 0.63
40–60	1.65 ± 0.02	6.15 ± 0.43	7.80 ± 0.44
60–88	1.36 ± 0.02	2.96 ± 0.18	4.32 ± 0.19
0–100	1.61 ± 0.01	6.84 ± 0.39	8.46 ± 0.39

B. Particle identification

Charged particle identification (PID) is performed by simultaneous measurement of the momentum, time of flight, and path length. These quantities are used to determine the mass of the candidate track based on the following relationship:

$$m^2 = \frac{p^2}{c^2}\left(\frac{t^2c^2}{L^2} - 1\right), \tag{1}$$

where m is the mass, p is the momentum, c is the speed of light, t is the time of flight, and L is the path length. The m^2 distributions are approximately Gaussian. The standard deviation of the distribution σ_{m^2} can be parametrized as a function of momentum as follows:

$$\sigma^2_{m^2} = \frac{\sigma^2_\alpha}{K_1^2}(4m^4p^2) + \frac{\sigma^2_{\rm ms}}{K_1^2}\left[4m^4\left(1+\frac{m^2}{p^2}\right)\right] + \frac{\sigma_t^2c^2}{L^2}[4p^2(m^2+p^2)], \tag{2}$$

where σ_{m^2} is the standard deviation of the m^2 distribution, m denotes the physical mass of the particle and thus the square root of the centroid of the m^2 distribution, σ_α is the angular resolution of the DC, $\sigma_{\rm ms}$ is the multiple scattering term, σ_t is the total timing resolution, and K_1 is the magnetic field integral constant. The magnetic field integral constant depends on the magnetic field configuration. The PHENIX magnet system for the central arms comprises two coils. The two coils can be run together, opposed, or have the inner coil off. During the 2007 Au + Au data taking, the coils were run opposed, while for the 2008 d + Au data taking, the coils were run together. Running the coils opposed produces near-zero magnetic fields in the region between the beam pipe and the inner coil of the magnet. This is needed for the analysis of the dielectron continuum using the hadron blind detector, which is the innermost detector during this operational period and can be seen (labeled as HBD) in Fig. 1. The PID parameters are presented in Table III.

TABLE III. Parameters for the PID function defined in Eq. (2).

Parameter	Units	2007 Au + Au	2008 d + Au
σ_α	mrad	0.896	1.050
$\sigma_{\rm ms}$	mrad GeV/c	0.992	1.000
σ_t	ps	0.084	0.095
K_1	mrad GeV/c	75.0	104.0

To select candidate tracks of a particular particle species, the m^2 is required to be within two standard deviations of the mean for the selected particle species and outside two standard deviations of the mean for the other particle species. Below the regions where the PID bands intersect, the PID contamination is negligible. Above it, contamination is from one side of the tail of the distribution beyond two standard deviations. For a Gaussian distribution this is 2.25%. Therefore, the contamination can be estimated based on the ratio of the respective yields multiplied by this value. The m^2 distributions may have slightly non-Gaussian tails and therefore the PID contamination may be slightly higher. In any event, we estimate the PID purity to be better than 90% for all particle species at all p_T, in all centrality classes, and in both collision systems. Figure 2 shows m^2 vs p_T multiplied by the charge for the 2007 Au + Au data; the 2008 d + Au data are very similar. The 2σ PID bands are superimposed as solid black lines. The top panel shows the entire m^2 distribution with all the track selection cuts applied but none of the PID cuts. The bottom panel shows the same distribution but with the PID cuts also applied.

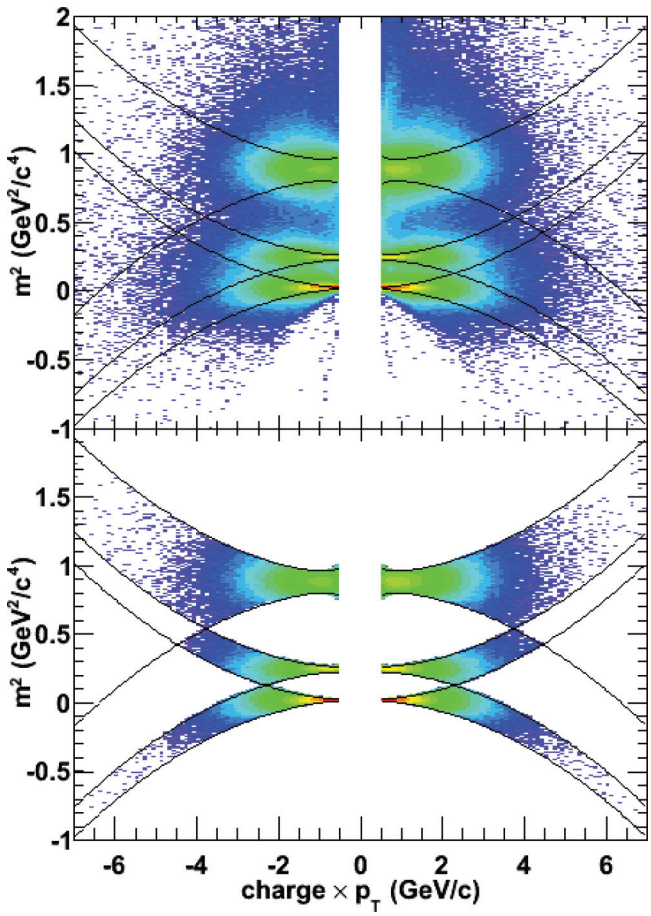

FIG. 2. (Color online) The particle identification method, m^2 vs charge × p_T for 2007 Au + Au data; the 2008 d + Au data are very similar. The solid black lines indicate the two-standard-deviation PID bands used for the cuts. The top panel shows the bands superimposed on the entire m^2 distribution; the bottom panel shows the distribution after the cuts have been applied.

C. Corrections to the raw data

To obtain the true invariant yield, the raw spectrum needs to be corrected for a variety of factors. Various types of simulations are performed to determine these corrections. To correct for geometrical acceptance, analysis cuts, particle interactions with detector materials, and in-flight decays (for pions and kaons), we use single-particle Monte Carlo (MC) simulations. For these simulations, single particles are generated using a random generator, with flat distributions in rapidity, azimuth, and p_T. The random particles are then run through a GEANT simulation of PHENIX to determine the interactions of the single particles with the detector subsystems and support structures. Next, all the detector response information is fed through the usual PHENIX reconstruction software to produce simulated tracks. Finally, these simulated tracks are analyzed in the exact same way as tracks from the real data to determine the corrections. The total correction factor, $F_C(p_T)$, is given by the following relation:

$$F_C(p_T) = \frac{dN_{\text{output}}/dp_T}{dN_{\text{input}}/dp_T} = \epsilon_{\text{acceptance}}\epsilon_{\text{efficiency}}\epsilon_{\text{cuts}}. \quad (3)$$

To correct for the detector occupancy effect, which is largest in the TOFW, we run embedding simulations, where a track from single-particle MC simulations is embedded into a real event, and the occupancy correction is determined from the relative efficiencies of reconstructing the single track in isolation and in the event. This correction is the largest in the most central Au + Au collisions, where the multiplicity is the highest and therefore the occupancy effect is the strongest. In the most peripheral Au + Au collisions the multiplicity is low enough that there is essentially no effect. The same is true in d + Au collisions, where no correction is applied.

For the d + Au system we apply a correction for the underlying event correlation that exists between produced particles measured in the central arms and particles at forward angles that satisfy the BBC interaction trigger [41]. This correlation produces both a trigger bias, in which events satisfying the trigger are biased towards higher multiplicities, and a bin shift, in which nominally peripheral events are shifted to higher centrality bins, thereby depleting the more peripheral bins. We correct for these effects using the Glauber MC combined with central particle yields measured in $p + p$ collisions. Using this same framework, we also generate a correction factor to convert the minimum-bias sample (0–88%) into one with zero bias (0–100%).

Table IV shows the centrality-dependent corrections for each collision species. The occupancy is represented as an efficiency, while the bias factor is represented as a multiplicative correction.

The proton and antiproton spectra are additionally corrected for the feed-down from weak decays of hyperons into protons. We use single-particle MC simulations of the Λ baryon and apply the analysis cuts used for the protons to determine the percentage of Λ baryons that decay into protons that pass our proton selection cuts. This is used to determine the percentage of the total proton sample that likely comes from hyperon decays, which is called the feed-down fraction.

TABLE IV. Summary of centrality-dependent corrections.

Collision	Centrality (%)	Occupancy-dependent efficiency
Au + Au	0–10	0.542
	10–20	0.653
	20–40	0.783
	40–60	0.904
	60–92	0.964
Collision	Centrality (%)	Bias-factor correction
d + Au	0–20	0.94
	20–40	1.00
	40–60	1.03
	60–88	1.03
	0–100	0.89

The feed-down fraction is dependent only on the Λ/p ratio and not explicitly on the Λ spectrum itself. For the Au + Au data we take the Λ/p ratio to be 0.89 and the $\bar{\Lambda}/\bar{p}$ ratio to be 0.95, as measured in Au + Au collisions at $\sqrt{s_{NN}} =$ 130 GeV [42]. These are very similar to (and well within the systematic uncertainties of) the values of 0.91 for Λ/p and 0.94 for $\bar{\Lambda}/\bar{p}$ obtained for Au + Au collisions at $\sqrt{s_{NN}} =$ 200 GeV by examining the dN/dy values for Λ and $\bar{\Lambda}$ [43] and p and $\bar{p}$ [10]. However, we note that the Λ data reported in Ref. [42] are inclusive while the data Λ reported in Ref. [43] are corrected for feed-down from other hyperons.

For the d + Au data, we take the Λ/p ratio to be 0.85 and the $\bar{\Lambda}/\bar{p}$ ratio to be 0.99. There are no published data on Λ/p and $\bar{\Lambda}/\bar{p}$ ratios or Λ and $\bar{\Lambda}$ spectra or yields in d + Au collisions that could be used to estimate these ratios. Instead, we use the $(\Lambda + \bar{\Lambda})/(p + \bar{p})$ ratio measured in $p + \bar{p}$ collisions [44], the $\bar{p}/p$ ratio measured in d + Au collisions [25], and an estimate of the $\bar{\Lambda}/\Lambda$ ratio in d + Au collisions based on measurements in Au + Au [45] and $p + p$ collisions [46].

The spectral shape of the Λ ($\bar{\Lambda}$) is assumed to follow the p ($\bar{p}$) spectrum with m_T scaling. We also take the ratio to be independent of centrality. In fact, a small centrality dependence can be seen when examining the integrated yields in Refs. [10, 43], although the different centralities are consistent within the systematic uncertainties.

All measurements of Λ implicitly include the Σ^0, which decays electromagnetically with 100% branching ratio to the Λ and a photon. We do not correct for feed-down from the charged Σ states, nor for the Ξ and Ω multistrange baryon states. Because these corrections are smaller and have large uncertainties, they are included in the overall systematic uncertainty estimates. For the charged Σ states we are concerned only with the Σ^+, which decays to a proton with a 0.5 branching ratio. The data from 200-GeV p+$\bar{p}$ collisions show a ratio $(\Sigma^+ + \Sigma^- + \bar{\Sigma}^+ + \bar{\Sigma}^-)/(\Lambda + \bar{\Lambda})$ of 0.50 ± 0.18(syst) [44]. Assuming $\bar{\Sigma}/\Sigma \approx \bar{\Lambda}/\Lambda$ and $\Sigma^-/\Sigma^+ \approx 1$, we can estimate Σ^+/Λ to be 0.25. The ratios for $(\Xi^0 + \bar{\Xi}^0)/(\Lambda + \bar{\Lambda})$ and $(\Xi^- + \bar{\Xi}^+)/(\Lambda + \bar{\Lambda})$ in $p + \bar{p}$ collisions both have a value of 0.065 with very large (≈100%) systematic uncertainties. Assuming $\bar{\Xi}/\Xi \approx \bar{\Lambda}/\Lambda$ one can estimate the $(\Xi^0 + \Xi^-)/\Lambda$ ratio to be roughly 0.13, which is consistent with the total feed-down correction of 15% reported for Λ in Ref. [43]. The latter also includes feed-down from Ω, though the contribution is small.

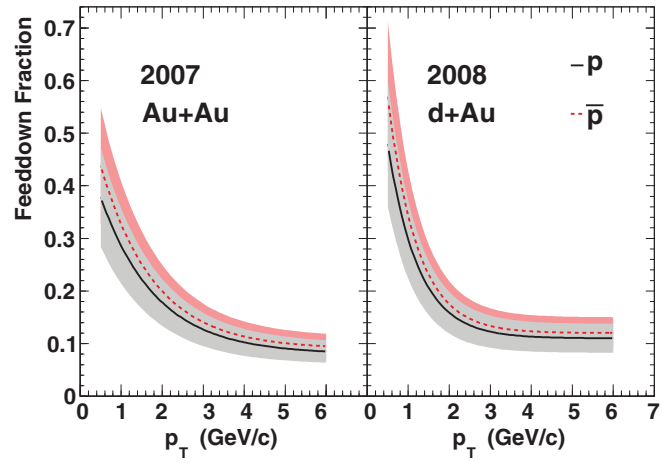

FIG. 3. (Color online) Feed-down fraction as a function of p_T for protons (solid black curves) and antiprotons (dotted red curves) for the 2007 Au + Au data (left panel) and the 2008 d + Au data (right panel). The shaded bands indicate the systematic uncertainty of 25%.

The systematic uncertainty on the feed-down fraction is estimated to be 25%, which is due primarily to the uncertainty in the Λ/p ratio. We also note that, in the p_T region of interest to this paper, $2\ \text{GeV}/c < p_T < 5\ \text{GeV}/c$, the feed-down fraction is of order 10%, so a 25% change in the Λ/p ratio produces only a roughly 2.5% change in the proton spectrum.

Figure 3 shows the feed-down fraction as a function of p_T for protons as solid black curves and antiprotons as dotted red curves for the 2007 Au + Au data (left panel) and 2008 d + Au data (right panel). As mentioned above, the magnetic field configuration is different for 2007 and 2008, which is the reason for the different feed-down fractions between the two data sets.

D. Estimation of systematic uncertainties

The different types of systematic uncertainty are categorized as follows: type A, point-to-point uncorrelated in p_T, where the points can move up or down independently of each other; type B, point-to-point correlated in p_T, where the points can move together, changing the shape of the curve; and type C, an overall normalization uncertainty in which all points move up or down by the same factor. The corrections for analysis cuts, including acceptance, track selection, and PID, are predominantly type B. The normalization corrections for effects such as detector occupancy and efficiency are type C. There are no known systematic uncertainties of type A in the present analysis. Typically type A systematic uncertainties come from the yield extraction of particles kinematically reconstructed from their decay products.

The uncertainties are assessed for each cut by redoing the analysis with the cut varied and then determining the difference. The cuts are varied in exactly the same way for the analysis of both the experimental and the simulated data. This process is repeated for all the analysis cuts and the differences are summed in quadrature to determine the final uncertainty. This is done for both the spectra and the ratios. The uncertainties are examined in each centrality class for both Au + Au and d + Au collisions and are found to be quite similar in all centrality classes.

TABLE V. Summary of systematic uncertainties from acceptance, track selection, and PID of invariant yield of each particle species.

p_T range	π^+ (%)	π^- (%)	K^+ (%)	K^- (%)	p (%)	$\bar{p}$ (%)
			2007 Au + Au			
$p_T < 3$ GeV/c	9	9	11	11	10	10
$p_T > 3$ GeV/c	10	10	11	11	11	11
$p_T > 5$ GeV/c	14	14	–	–	14	14
			2008 d + Au			
$p_T < 3$ GeV/c	8	8	13	13	9	9
$p_T > 3$ GeV/c	9	9	13	13	11	11

When taking ratios of the various particles, all of the type C uncertainties and some of the type B uncertainties cancel. For antiparticle-to-particle ratios, the uncertainty from acceptance does not cancel at all, and the uncertainty from track selection and PID mostly cancel. For other particle ratios, K/π and p/π, the uncertainty from acceptance and track selection mostly cancel, and the uncertainty from PID does not cancel at all. In this analysis, we find the remaining systematic uncertainty on each of the particle ratios is roughly 5% for all p_T.

For the nuclear modification factor R_{CP}, which compares two different centrality bins of the same particle species in the same collision system, all the type B systematic uncertainties cancel almost completely. There is an uncertainty of about 2% based on small variations of the track matching and PID distributions as a function of centrality. The type C uncertainties are completely uncorrelated and added in quadrature. For the nuclear modification factors R_{AA} and R_{dA}, the $p + p$ reference data were collected during a different operational period and using different detector subsystems; therefore, none of the systematic uncertainties cancel. A summary of the type B systematic uncertainties for the spectra is given in Table V.

The type C uncertainties are from the centrality-dependent corrections for the spectra and from the uncertainty on the Glauber model calculations for the nuclear modification factors. The uncertainty on the occupancy correction for Au + Au collisions is roughly 10%, and therefore the uncertainty on the yield varies from 5% for the most central to less than 1% for the most peripheral. The uncertainties for the Glauber values for $N_{\rm coll}$ are much larger and therefore dominate the uncertainty in the nuclear modification factors.

The uncertainty on the bias factors for d + Au collisions varies from about 1% for the most central bin to about 5% for the most peripheral bin. The bias factors are determined in the same Glauber model analysis as the $N_{\rm coll}$ and $N_{\rm part}$ values, and therefore the uncertainties are correlated. The uncertainty on the ratio of bias factors and $N_{\rm coll}$ values used to determine the nuclear modification factors varies from about 3% for the most central to about 8% for the most peripheral.

IV. RESULTS AND DISCUSSION

A. Invariant yields as a function of transverse momentum p_T

The main result of this study is the measurement of the invariant yield of pions, kaons, and protons as a function of p_T in different centrality classes. The centrality classes studied in the Au + Au measurement are 0–10% (the most central), 10–20%, 20–40%, 40–60%, and 60–92% (the most peripheral). For the d + Au measurement, the centrality classes are 0–20% (the most central), 20–40%, 40–60%, 60–88% (the most peripheral), and 0–100%. From these quantities, all other observables are derived, such as particle ratios and nuclear modification factors. Figure 4 shows the invariant yields of positive pions, positive kaons, and protons (top left, middle, and right, respectively) and negative pions, negative kaons, and antiprotons (bottom left, middle, and right, respectively). The yields are scaled by arbitrary factors indicated in the legend for the sake of clarity and to keep the collision species grouped together. The plotted invariant yields are available in Tables I–XII of the Supplemental Material [47]. These spectra are consistent with previously published PHENIX spectra [10,25] in the overlapping p_T range.

B. Particle ratios as a function of transverse momentum

One of the simpler classes of derived quantities is the antiparticle-to-particle ratio. In the present analysis those ratios are π^-/π^+, K^-/K^+, and $\bar{p}/p$, which are plotted as a function of p_T in the upper, middle, and lower panels of Fig. 5, respectively. In each panel, the Au + Au data are on the left and the d + Au data are on the right. Drawn as a visual aid are dashed black lines with value 1.0 for the pions, 0.93 for the kaons, and 0.73 for the protons; the values for kaons and protons are chosen from the reported p_T integrated values from Ref. [10]. Shown as a reference are data from $p + p$ collisions from Ref. [48] for $p_T < 3$ GeV/c and from Ref. [49] for $p_T > 3$ GeV/c. Remarkably, all the ratios are essentially independent of both p_T and centrality. Based on simple arguments about isospin conservation and the basics of the parton distribution functions and fragmentation functions, one would expect each of the antiparticle-to-particle ratios to vary as a function of p_T as discussed in Ref. [50]. Indeed, these ratios have a significant p_T dependence in $p + p$ collisions at midrapidity, and the agreement with theory depends significantly on the fragmentation functions used [49]. However, the p_T range needed to observe the decrease in these ratios in $p + p$ collisions is quite large. As seen in Fig. 5, the p_T dependence of the ratios in $p + p$ is small over the range measured and is consistent with the ratios in d + Au and Au + Au.

Figures 6 and 7 show the kaon-to-pion ratios as a function of (top) p_T K^+/π^+ and (bottom) K^-/π^- in Au + Au and d + Au collisions, respectively. The ratios in Au + Au collisions show a significant increase with increasing p_T and a small increase as the collisions become more central. The enhancement of the integrated K/π ratio in more central collisions is attributed to strangeness equilibration in various thermal models [51,52], which is reflected in the differential ratio. However, the differential ratio may include additional information about the differences in the fragmentation functions and/or the phase-space distribution functions used in the recombination models. As discussed in a previous PHENIX publication [53], the strangeness enhancement present in the hot and dense nuclear medium has an effect on certain recombination models [54]. These models involve the recombination of partons in dissimilar

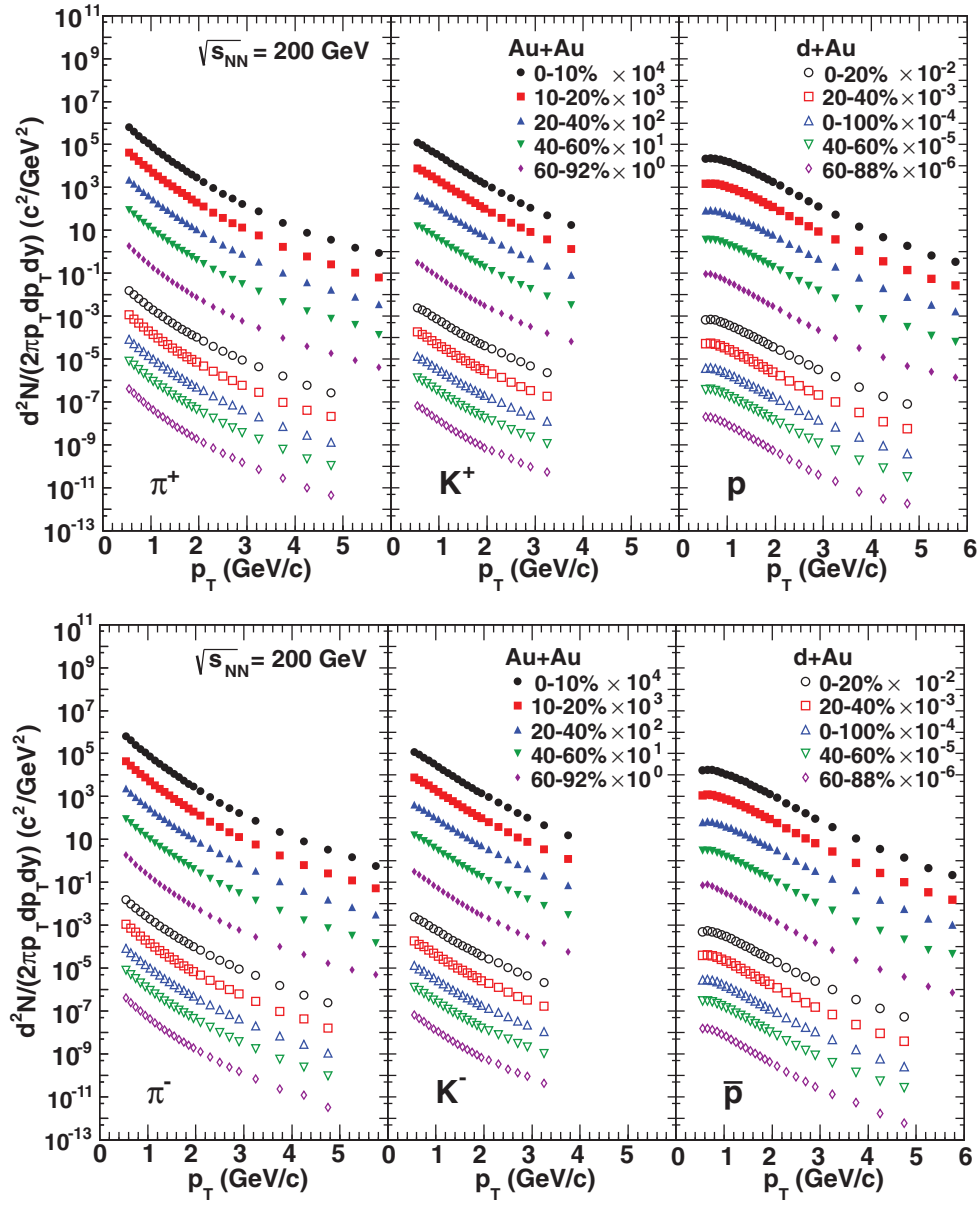

FIG. 4. (Color online) Invariant yield of $\pi^{\pm}$, $K^{\pm}$ and p and $\bar{p}$ as a function of p_T in Au + Au and d + Au collisions. The yields are scaled by the arbitrary factors indicated in the legend, keeping collision species grouped together. Statistical uncertainties are too small to be seen. Systematic uncertainties are discussed in Table V. The tabulated values are available in Tables I–XII of the Supplemental Material [47].

momentum space, meaning that a shower parton from a jet can recombine with a thermal parton in the medium. The thermal component of thermal + shower recombination is more dominant at higher p_T for strange hadrons (such as kaons) than it is for nonstrange hadrons (such as pions), leading to an enhancement of the ratio that increases with p_T. This increasing enhancement manifests as the ratio rising more quickly in Au + Au collisions compared with $p + p$ collisions, which is seen in Figs. 6 and 7. At sufficiently high p_T, where the shower component begins to dominate for both strange and nonstrange particles, this ratio is expected to turn over and begin to decrease. However, this turnover point, if it exists, is beyond the p_T reach available for kaons in this study.

The K/π ratios in d + Au collisions are essentially identical for all centrality classes, which may indicate that the mechanism for strangeness production in d + Au collisions is the same for all centrality classes. However, we also note that the various d + Au centrality classes span a relatively small range of N_{part}. Therefore, if the strangeness enhancement is only weakly dependent on N_{part}, the variation of N_{part} in the d + Au centrality classes may not be large enough for an effect to be observed.

Figures 8 and 9 show the proton-to-pion ratios as a function of p_T (p/π^+ on the top, $\bar{p}/\pi^-$ on the bottom) in Au + Au and d + Au collisions, respectively. Note that for Fig. 9 the vertical scale is different. The ratios in central Au + Au collisions show a strong enhancement over the values in $p + p$ collisions. This

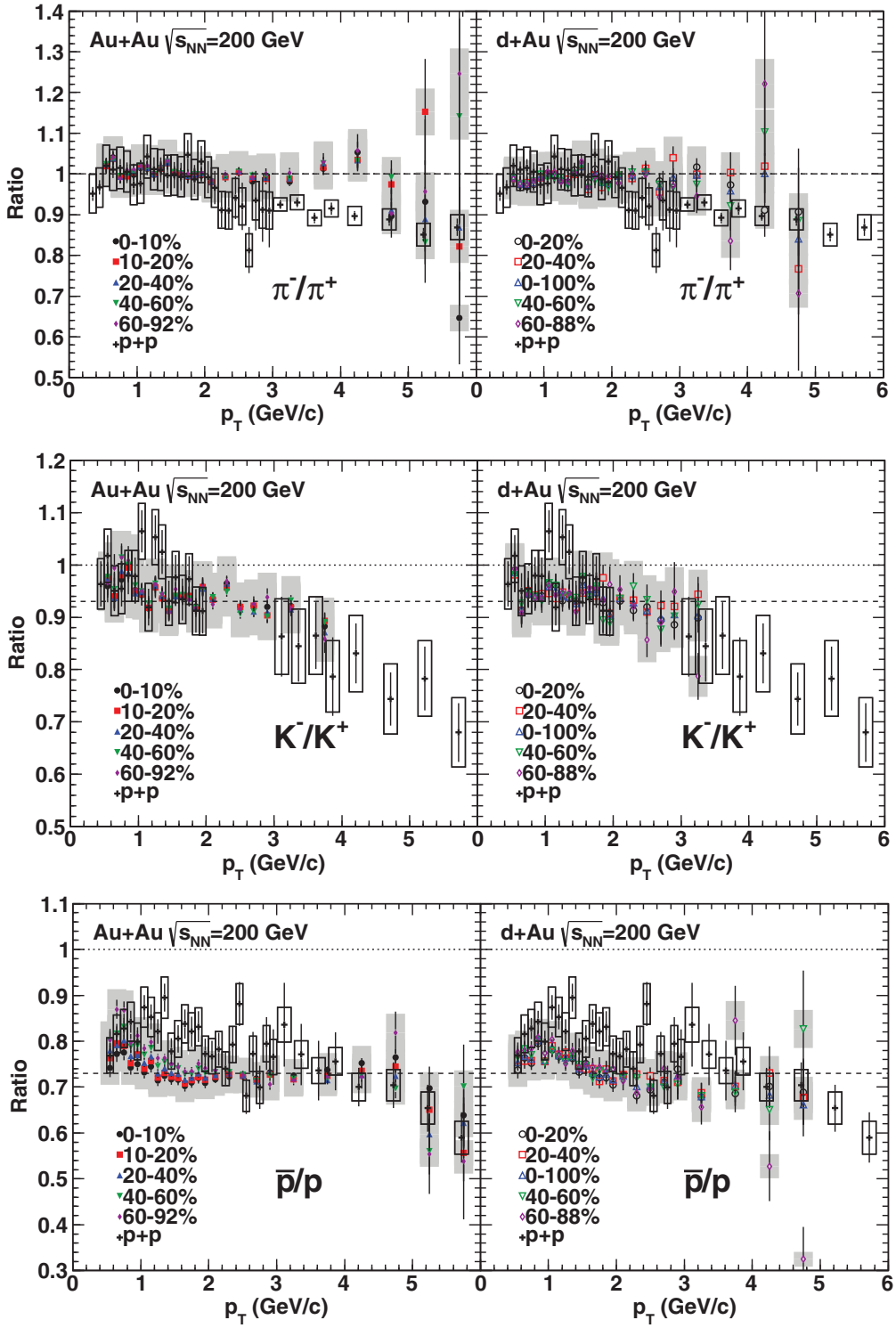

FIG. 5. (Color online) Ratio of invariant yield of π^-/π^+ (top), K^-/K^+ (middle), and $\bar{p}/p$ (bottom) as a function of p_T in Au + Au (left panels) and d + Au collisions (right panels) in each centrality bin. Dashed lines are drawn as a visual aid with values of 1.0 for π^-/π^+, 0.93 for K^-/K^+, and 0.73 for $\bar{p}/p$. These values are taken from Ref. [10]. Shown as a reference are data from $p + p$ collisions from Ref. [48] for $p_T < 3$ GeV/c and from Ref. [49] for $p_T > 3$ GeV/c.

is conjectured to be attributed to the parton recombination mechanism of hadronization, which gives rise to a significant enhancement of baryon yields relative to meson yields in heavy-ion collisions [16,18,20]. The p/π ratios in the other centralities in Au + Au collisions show a clear and consistent trend with decreasing enhancement as the collisions become more peripheral. In d + Au collisions there is a similar trend. The p/π ratio in the most central d + Au collisions appears

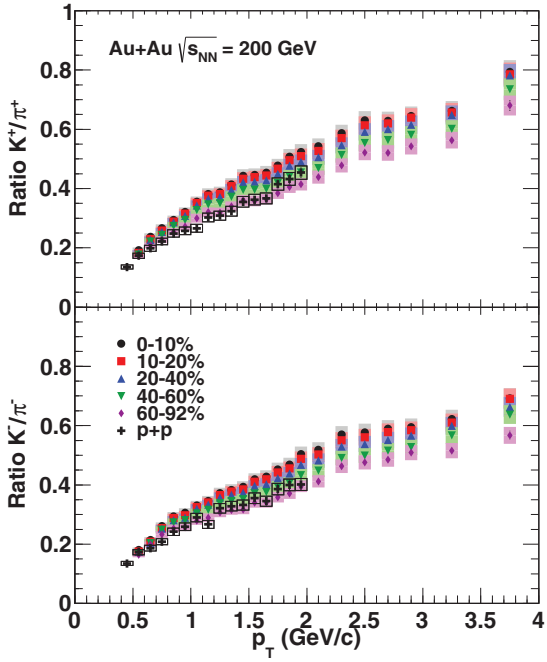

FIG. 6. (Color online) Ratio of invariant yield of positive kaons to positive pions (top panel) and negative kaons to negative pions (bottom panel) as a function of p_T in Au + Au collisions in the centrality bins marked in the legend. Data for $p + p$ collisions [48] are shown as a reference.

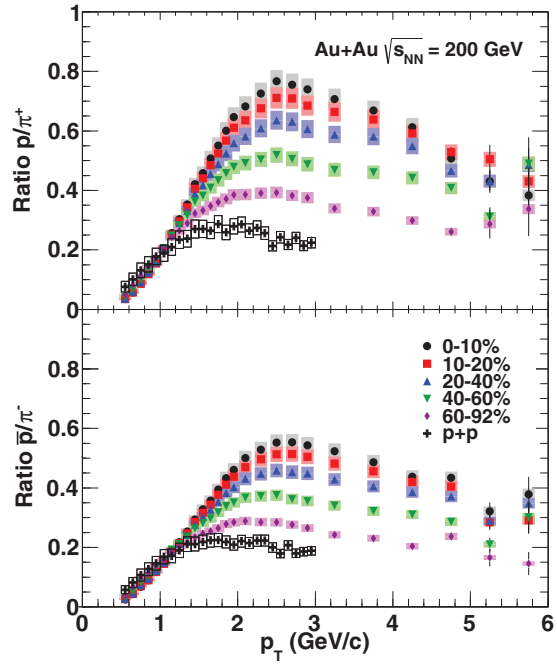

FIG. 8. (Color online) Ratio of invariant yield of protons to positive pions (top panel) and antiprotons to negative pions (bottom panel) as a function of p_T in Au + Au collisions in the centrality bins marked in the legend. Data for $p + p$ collisions [48] are shown as a reference.

to be consistent with the ratio in the most peripheral Au + Au collisions. Additionally, the p/π ratio is enhanced over $p + p$ collisions for each centrality class in d + Au collisions except for the most peripheral.

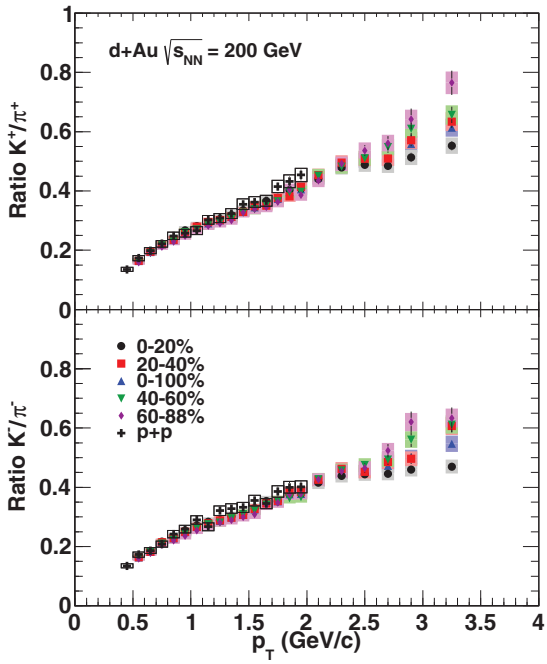

FIG. 7. (Color online) Ratio of invariant yield of positive kaons to positive pions (top panel) and negative kaons to negative pions (bottom panel) as a function of p_T in d + Au collisions in the centrality bins marked in the legend. Data for $p + p$ collisions [48] are shown as a reference.

C. Nuclear modification factors as a function of transverse momentum

To measure the modification of the spectrum of produced particles in heavy-ion collisions relative to the spectrum in $p + p$ collisions, nuclear modification factors are employed. The nuclear modification factor R_{AA} is defined as the yield in Au + Au collisions divided by the yield in $p + p$ collisions, normalized by the number of binary nucleon + nucleon collisions $N_{\rm coll}$, as determined from the Glauber model. The nuclear modification factor R_{CP} is defined as the yield in central Au + Au collisions divided by the yield in peripheral Au + Au collisions, normalized to the respective numbers of binary nucleon + nucleon collisions. These can be expressed mathematically as

$$R_{AA} = \frac{(dN/dp_T)^{\rm Au+Au}}{N_{\rm coll}^{\rm Au+Au}(dN/dp_T)^{p+p}}, \tag{4}$$

$$R_{CP} = \frac{(dN/dp_T)^{\rm central}}{(dN/dp_T)^{\rm peripheral}} \frac{N_{\rm coll}^{\rm peripheral}}{N_{\rm coll}^{\rm central}}. \tag{5}$$

Figure 10 shows R_{CP} for 0–10%/40–60% (left panel) and 0–10%/60–92% (right panel) as a function of p_T for charge-averaged pions, kaons, and protons. Both pions and kaons exhibit a suppression pattern at all values of p_T. The kaons exhibit less suppression than the pions, indicating the additional role of strangeness enhancement in the particle-production

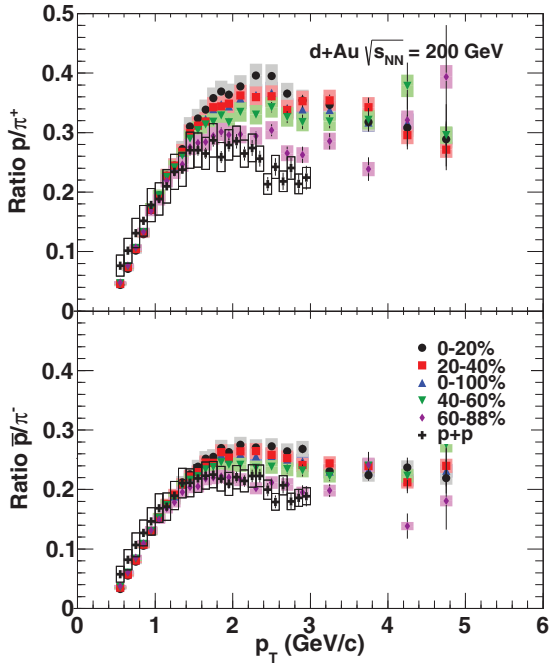

FIG. 9. (Color online) Ratio of invariant yield of protons to positive pions (top panel) and antiprotons to negative pions (bottom panel) as a function of p_T in $d + \mathrm{Au}$ collisions in the centrality bins marked in the legend. Data for $p + p$ collisions [48] are shown as a reference.

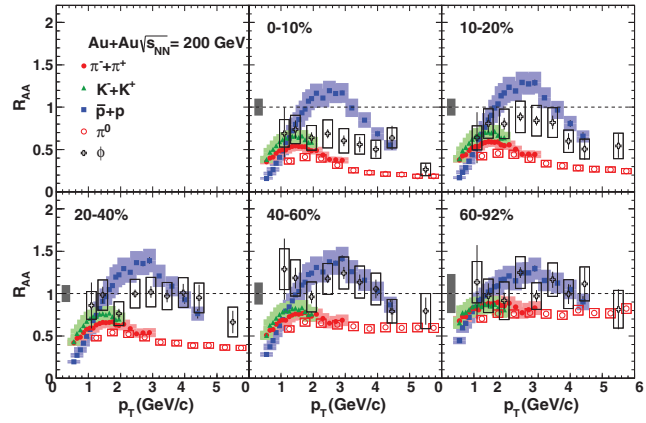

FIG. 11. (Color online) Nuclear modification factor R_{AA} as a function of p_T in different centrality classes of charge-averaged pions, kaons, and protons, π^0 [55], and ϕ [53]. A dashed black line is drawn at unity as a visual aid, indicating no modification. The shaded gray boxes indicate the associated uncertainty on N_{coll} from the Glauber model calculations. The tabulated values are available in Tables XIII–XV of the Supplemental Material [47].

mechanism. The observed enhancement of kaons relative to pions appears to be lower for the 0–10%/40–60% as compared to the 0–10%/60–92%, suggesting a centrality dependence of the strangeness enhancement, as seen in the K/π ratios discussed above. However, the protons exhibit quite different behavior, rising to a value very close to unity, indicating no suppression, around 2–3 GeV/c in p_T. At higher values of p_T the proton R_{CP} falls off slowly, beginning to approach the pion R_{CP} at the highest values of p_T available. The proton R_{CP} shown here is consistent within the systematic uncertainties with the proton R_{CP} reported by STAR [57].

Figure 11 shows R_{AA} as a function of p_T in different centrality classes for charge-averaged pions, kaons, and protons, as well for π^0 [55] and ϕ [53]. We use previously published PHENIX data on identified hadrons in $p + p$ collisions [48] to evaluate the R_{AA}. The R_{AA} data are limited in p_T reach by the $p + p$ data. As with the R_{CP}, the pions and kaons exhibit a suppression pattern in the R_{AA}. Additionally, a significant and monotonic centrality dependence is observed, with the suppression decreasing as the collisions become more peripheral. This is consistent with what is seen for neutral pions [55,58]. The proton R_{AA} shows no suppression in the intermediate p_T region and in fact reaches a maximum value above unity between 2 and 3 GeV/c. For $p_T > 3$ GeV/c, the proton R_{AA} values decrease and a suppression pattern emerges. The proton R_{CP} decreases more slowly than the central proton R_{AA}, which is simply because of the still considerable modification in the peripheral bins. The trend appears to be that the proton R_{CP} and R_{AA} decrease steadily while the pion R_{CP} and R_{AA} hold steady, suggesting that these values for pions and protons may eventually merge. The proton R_{AA} for the 0–10% centrality bin shown here exhibits reasonable qualitative agreement with the $K + p$ R_{AA} for 0–12% centrality reported by STAR [49].

While the centrality dependence of the R_{AA} for the pions and kaons is strong, it is quite weak for the protons and the different centralities are consistent within the systematic uncertainties. This is consistent with the strong centrality

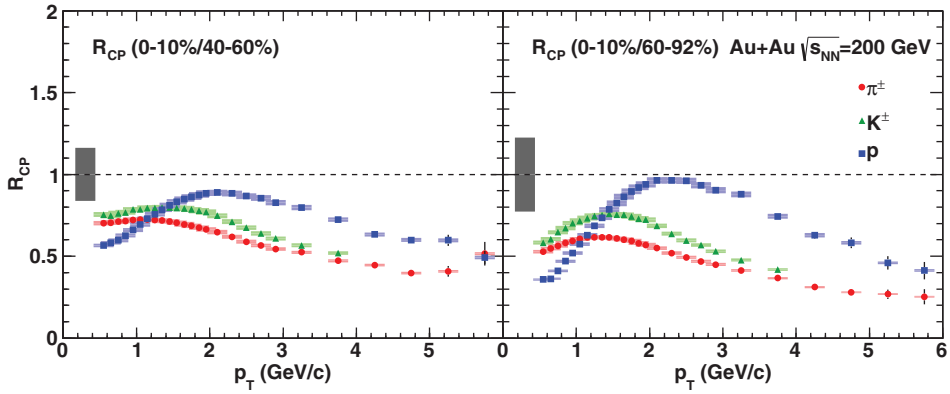

FIG. 10. (Color online) R_{CP} for 0–10%/40–60% (left panel) and 0–10%/60–92% (right panel) as a function of p_T for charge-averaged pions, kaons, and protons. A dashed black line is drawn at unity as a visual aid, indicating no modification. The shaded gray boxes indicate the associated uncertainty on N_{coll} from the Glauber model calculations.

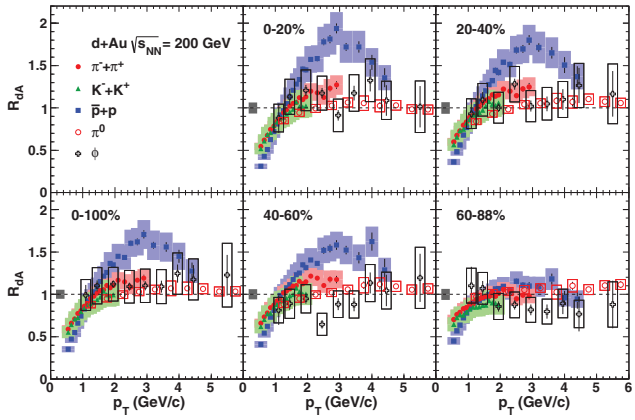

FIG. 12. (Color online) Nuclear modification factor R_{dA} as a function of p_T in different centrality classes of charge-averaged pions, kaons, and protons, π^0 [56], and ϕ [53]. A dashed black line is drawn at unity as a visual aid, indicating no modification. The shaded gray boxes indicate the associated uncertainty on $N_{\rm coll}$ from the Glauber model calculations. The tabulated values are available in Tables XVI–XVIII of the Supplemental Material [47].

dependence in the p/π ratios discussed above. The ϕ meson $R_{\rm AA}$ values are close to the values for kaons and significantly lower than the values for the protons, even though the ϕ is much heavier than the kaon and it has roughly the same mass as the proton. This strongly suggests a baryon vs meson dynamic, as opposed to a simple mass dependence, as would be the case for radial flow developed during the hadronic phase.

The nuclear modification factor for d + Au collisions, R_{dA}, is defined in a similar way as $R_{\rm AA}$ by

$$R_{dA} = \frac{(dN/dp_T)^{d+\rm Au}}{N_{\rm coll}^{d+\rm Au}(dN/dp_T)^{p+p}}. \quad (6)$$

Figure 12 shows R_{dA} as a function of p_T in different centrality classes for charged averaged particles. As with the $R_{\rm AA}$, we use previously published PHENIX data on identified hadrons in $p+p$ collisions [48] to evaluate the R_{dA}. The $p+p$ data limit the p_T reach of the R_{dA}. The charged pion exhibits a small modification above p_T of 1.0 GeV/c and is consistent with no modification within the systematic uncertainties. This is consistent with previous measurements of neutral pions [56,59]. The charged kaon agrees with the charged pion within the systematic uncertainties. The ϕ meson exhibits no apparent modification.

However, the protons show a very large and strongly centrality-dependent Cronin enhancement, reaching a factor of 2 in the most central collisions at intermediate p_T. Even in the 40–60% centrality class the enhancement is a factor of 1.5. For the most peripheral bin the enhancement is much smaller, at a factor of about 1.1–1.2, and is close to unmodified, similar to the other particle species. This strong centrality dependence of the proton R_{dA} is, in fact, very similar to the significant centrality dependence of the p/π ratio, and these two observables are likely driven by the same mechanism. Also apparent in the R_{dA} is that the enhancement for protons begins to fall off at 3.0 GeV/c and steadily drops with increasing p_T, appearing nearly unmodified at the highest p_T points.

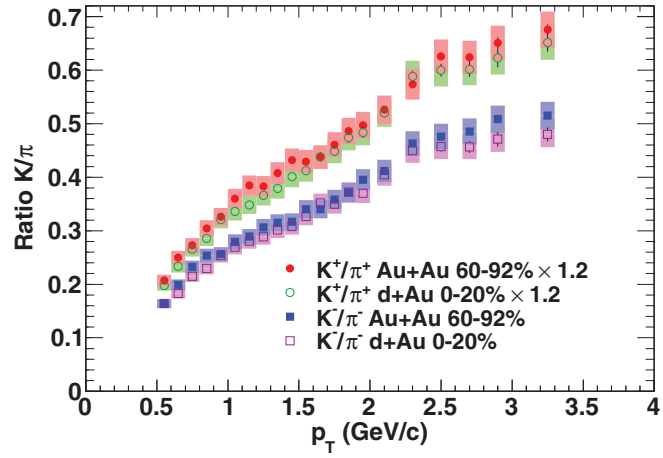

FIG. 13. (Color online) Ratio of K^+/π^+ and K^-/π^- as a function of p_T in peripheral Au + Au and central d + Au collisions plotted together. The K^+/π^+ ratios have been scaled by a factor of 1.2 for the sake of clarity.

The R_{dA} of π, K, ϕ, and p show significant dependence on the number of valence quarks and no dependence on particle mass. That the baryon R_{dA} is quite different from that of the mesons suggests that recombination plays a role in particle production in d + Au collisions as well as Au + Au. The kaon R_{dA} is consistent with the pion R_{dA}, in contrast to $R_{\rm AA}$ where the kaons are consistently above the pions. This is consistent with the K/π ratio discussed above and indicates that there is no discernible strangeness enhancement within uncertainties in d + Au collisions.

D. Comparison of peripheral Au + Au to central d + Au

Motivated by the remarkable similarities between peripheral Au + Au and central d + Au collisions, we now compare the two directly. Figure 13 shows the K/π ratio and Fig. 14 shows the p/π ratio in peripheral Au + Au

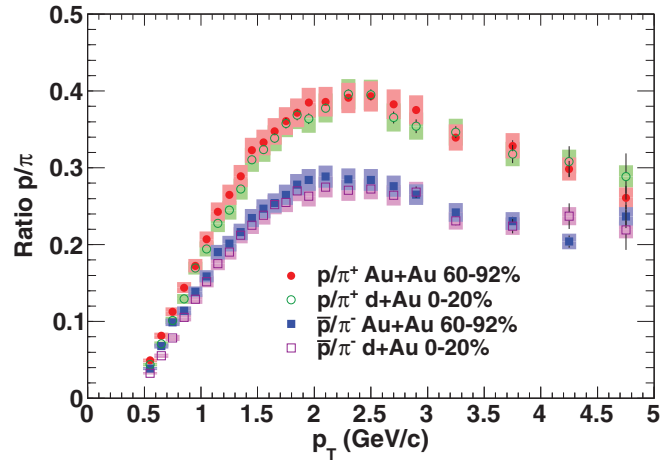

FIG. 14. (Color online) Ratio of p/π^+ and $\bar{p}/\pi^-$ as a function of p_T in peripheral Au + Au and central d + Au collisions plotted together.

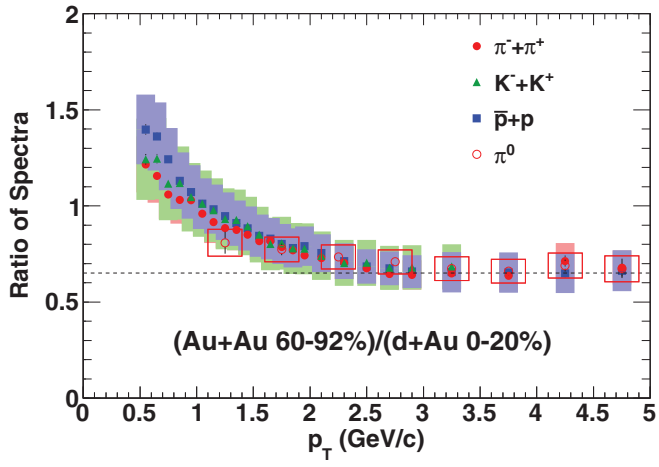

FIG. 15. (Color online) Ratio of invariant yield of particles in peripheral Au + Au (60–92%) to central d + Au (0–20%) collisions as a function of p_T.

and central d + Au collisions plotted together. In both cases the ratios are completely consistent with each other between the different collision species, suggesting that the particle-production mechanisms in peripheral Au + Au and central d + Au collisions are quite similar.

Figure 15 shows the ratio of the spectra in peripheral Au + Au to central d + Au collisions for pions, kaons, and protons. Also plotted is the ratio for neutral pions, as determined from the data in Refs. [55,56]. The ratio for π^0 shows excellent agreement with the $\pi^{\pm}$ ratios.

We note that the $N_{\rm coll}$ and $N_{\rm part}$ values are quite consistent with each other. The ratio of $N_{\rm coll}$ in 0–20% d + Au to $N_{\rm coll}$ in 60–92% Au + Au is 1.02 ± 0.22, and the same ratio for the respective $N_{\rm part}$ values is 1.04 ± 0.21. No scaling is applied, but a scaling by the respective $N_{\rm coll}$ or $N_{\rm part}$ values would change the data imperceptibly. The ratios tend to the same value of roughly 0.65 for each particle species at and above 2.5–3 GeV/c. This universal scaling is strongly suggestive of a common particle-production mechanism between peripheral Au + Au and central d + Au collisions. It is also interesting to observe that at the lower p_T, where this ratio rises strongly, there is minimal mass or particle-type dependence.

Given the fact that both $N_{\rm coll}$ and $N_{\rm part}$ are essentially the same in these two systems, any quantity or physical effect that scales with either of these should be the same in each system, and thus should cancel almost exactly in this ratio. If we make the simple assumption that most or all of the cold-nuclear-matter effects scale with $N_{\rm coll}$ or $N_{\rm part}$, then those effects are completely canceled in this ratio, leaving only the hot-nuclear-matter effects present in the peripheral Au + Au collisions. This could mean that this ratio being less than unity is attributable to the parton energy loss in peripheral Au + Au. This picture is consistent with the findings in this paper and elsewhere that the $R_{\rm AA}$ of mesons indicates parton energy loss in the medium even in peripheral Au + Au collisions. It is striking, then, that this ratio is independent of particle species, which is suggestive of similar energy loss effects even for protons. This indicates that the baryon enhancement mechanism is the same in both systems.

However, although $N_{\rm coll}$ and $N_{\rm part}$ are consistent for the two systems, there is an inherent participant asymmetry that needs to be taken into account. In the case of peripheral Au + Au collisions, one has a scenario in which, for example, 7 or 8 nucleons on the edge of one Au nucleus collide against 7 or 8 nucleons on the edge of the other Au nucleus. However, in the case of central d + Au collisions, one has a scenario in which, for example, the 2 nucleons of the deuteron collide against 13 nucleons in the center of the Au nucleus. This introduces several additional factors that need to be considered. For example, the participant asymmetry produces a rapidity shift in the particle production [60]. This may explain a deficit of soft particles at low p_T in d + Au collisions at midrapidity, which, in turn, would explain why the ratio trends up at low p_T. We also note this low-p_T region where the ratio rises is where hydrodynamics effects are known to be important in Au + Au collisions. It is possible that there are collective flow effects in d + Au collisions as well, as suggested by the recent results reported in Refs. [26–29]. A full viscous hydrodynamics model comparison is warranted.

Another issue to consider is the modification of parton distribution functions (PDFs) in nuclei. These nuclear PDFs (nPDFs) are known to be modified from the PDFs of single nucleons [7,61]. The experimentally measured nPDFs are averaged over the entire nucleus and are typically compared to the deuteron PDF to determine the nuclear modification. The binary collisions in peripheral Au + Au involve two nucleons which have modified nPDFs. However, the binary collisions in central d + Au involve an approximately unmodified nucleon from the deuteron and a modified nucleon from the Au nucleus. Physical observables sensitive to the nPDFs would then be expected to be different for the two systems. However, it is possible that the nucleons in the more diffuse outer region of the nucleus have a different modification from those in the denser center. Therefore, it is not possible to make any model-independent quantitative statements about the differences between the nPDFs in these two systems.

V. SUMMARY

In summary, we present a highly detailed and systematic study of identified charged hadron spectra and ratios as a function of p_T and centrality for Au + Au and d + Au collisions at $\sqrt{s_{NN}} = 200$ GeV. As has been reported previously, we find a baryon enhancement present in both systems. In d + Au collisions, the Cronin enhancement has long been known to be stronger for baryons than for mesons. However, for the first time a study with enough statistical and systematic precision presents clear evidence for a strong centrality dependence of this effect. In Au + Au collisions the baryon enhancement has been attributed to parton recombination as the mode of hadronization. A version of the recombination model has been applied to d + Au collisions as well [22,23], which reproduces the baryon vs meson differences. The present data strongly suggest that further theoretical investigation is warranted. Given the excellent statistical precision of the present data set, a direct comparison between the two is made for the first time. Specifically, a ratio of the spectra in the most peripheral

Au + Au and most central d + Au collisions is measured. These two systems have nearly identical values of both $N_{\rm coll}$ and $N_{\rm part}$. Therefore, a direct comparison between the two cancels out a large number of physical effects. We conclude that the baryon enhancement present in both systems is likely driven by a common hadronization mechanism.

ACKNOWLEDGMENTS

We thank the staff of the Collider-Accelerator and Physics Departments at Brookhaven National Laboratory and the staff of the other PHENIX participating institutions for their vital contributions. We acknowledge support from the Office of Nuclear Physics in the Office of Science of the Department of Energy, the National Science Foundation, Abilene Christian University Research Council, Research Foundation of SUNY, and the Dean of the College of Arts and Sciences, Vanderbilt University (USA); Ministry of Education, Culture, Sports, Science, and Technology and the Japan Society for the Promotion of Science (Japan); Conselho Nacional de Desenvolvimento Científico e Tecnológico and Fundação de Amparo à Pesquisa do Estado de São Paulo (Brazil); Natural Science Foundation of China (People's Republic of China); Ministry of Education, Youth and Sports (Czech Republic); Centre National de la Recherche Scientifique, Commissariat à l'Énergie Atomique, and Institut National de Physique Nucléaire et de Physique des Particules (France); Bundesministerium für Bildung und Forschung, Deutscher Akademischer Austausch Dienst, and Alexander von Humboldt Stiftung (Germany); Hungarian National Science Fund, OTKA (Hungary); Department of Atomic Energy and Department of Science and Technology (India); Israel Science Foundation (Israel); National Research Foundation and the WCU program of the Ministry Education Science and Technology (Korea); Ministry of Education and Science, Russian Academy of Sciences, Federal Agency of Atomic Energy (Russia); VR and Wallenberg Foundation (Sweden); the US Civilian Research and Development Foundation for the Independent States of the Former Soviet Union; the US-Hungarian Fulbright Foundation for Educational Exchange; and the US-Israel Binational Science Foundation.

[1] K. Adcox *et al.* (PHENIX Collaboration), Nucl. Phys. A **757**, 184 (2005).
[2] J. Adams *et al.* (STAR Collaboration), Nucl. Phys. A **757**, 102 (2005).
[3] B. B. Back *et al.* (PHOBOS Collaboration), Nucl. Phys. A **757**, 28 (2005).
[4] I. Arsene *et al.* (BRAHMS Collaboration), Nucl. Phys. A **757**, 1 (2005).
[5] J. W. Cronin, H. J. Frisch, M. J. Shochet, J. P. Boymond, R. Mermod *et al.*, Phys. Rev. D **11**, 3105 (1975).
[6] D. Antreasyan, J. W. Cronin, H. J. Frisch, M. J. Shochet, L. Kluberg, P. A. Piroue, and R. L. Sumner, Phys. Rev. D **19**, 764 (1979).
[7] M. Arneodo, Phys. Rep. **240**, 301 (1994).
[8] E. Iancu and R. Venugopalan, in *Quark-Gluon Plasma 3*, edited by R. C. Hwa and X.-N. Wang (World Scientific, Singapore, 2004), p. 249.
[9] S. S. Adler *et al.* (PHENIX Collaboration), Phys. Rev. Lett. **91**, 172301 (2003).
[10] S. S. Adler *et al.* (PHENIX Collaboration), Phys. Rev. C **69**, 034909 (2004).
[11] J. Adams *et al.* (STAR Collaboration), Phys. Rev. Lett. **92**, 052302 (2004).
[12] U. Heinz *et al.*, Nucl. Phys. A **702**, 269 (2002).
[13] T. Hirano and Y. Nara, Phys. Rev. C **69**, 034908 (2004).
[14] I. Vitev and M. Gyulassy, Phys. Rev. C **65**, 041902 (2002).
[15] I. Vitev and M. Gyulassy, Nucl. Phys. A **715**, 779 (2003).
[16] R. C. Hwa and C. B. Yang, Phys. Rev. C **67**, 034902 (2003).
[17] R. J. Fries, B. Muller, C. Nonaka, and S. A. Bass, Phys. Rev. Lett. **90**, 202303 (2003).
[18] R. J. Fries, B. Muller, C. Nonaka, and S. A. Bass, Phys. Rev. C **68**, 044902 (2003).
[19] V. Greco, C. M. Ko, and P. Levai, Phys. Rev. Lett. **90**, 202302 (2003).
[20] V. Greco, C. M. Ko, and P. Levai, Phys. Rev. C **68**, 034904 (2003).
[21] D. Molnar and S. A. Voloshin, Phys. Rev. Lett. **91**, 092301 (2003).
[22] R. C. Hwa and C. B. Yang, Phys. Rev. Lett. **93**, 082302 (2004).
[23] R. C. Hwa and C. B. Yang, Phys. Rev. C **70**, 037901 (2004).
[24] A. Accardi, arXiv:hep-ph/0212148.
[25] S. S. Adler *et al.* (PHENIX Collaboration), Phys. Rev. C **74**, 024904 (2006).
[26] A. Adare *et al.* (PHENIX Collaboration), arXiv:1303.1794.
[27] S. Chatrchyan *et al.* (CMS Collaboration), Phys. Lett. B **718**, 795 (2013).
[28] B. Abelev *et al.* (ALICE Collaboration), Phys. Lett. B **719**, 29 (2013).
[29] G. Aad *et al.* (ATLAS Collaboration), Phys. Rev. Lett. **110**, 182302 (2013).
[30] S. A. Bass *et al.*, Nucl. Phys. A **661**, 205 (1999).
[31] J. Rafelski and B. Muller, Phys. Rev. Lett. **48**, 1066 (1982).
[32] P. Koch and B. Muller, Phys. Rep. **142**, 167 (1986).
[33] K. Adcox *et al.* (PHENIX Collaboration), Nucl. Instrum. Methods A **499**, 469 (2003).
[34] K. Ikematsu *et al.*, Nucl. Instrum. Methods A **411**, 238 (1998).
[35] M. Allen *et al.* (PHENIX Collaboration), Nucl. Instrum. Methods A **499**, 549 (2003).
[36] V. G. Ryabov, Nucl. Instrum. Methods A **419**, 363 (1998).
[37] J. Barrette *et al.*, Nucl. Phys. A **661**, 665 (1999).
[38] B. Love, Masters thesis, Vanderbilt University, 2009, http://www.phenix.bnl.gov/WWW/talk/archive/theses/2009/Love_Brian-thesis_BrianLove.pdf.
[39] A. Adare *et al.* (PHENIX Collaboration), Phys. Rev. C **85**, 064914 (2012).
[40] M. L. Miller, K. Reygers, S. J. Sanders, and P. Steinberg, Annu. Rev. Nucl. Part. Sci. **57**, 205 (2007).
[41] S. S. Adler *et al.* (PHENIX Collaboration), Phys. Rev. Lett. **94**, 082302 (2005).
[42] K. Adcox *et al.* (PHENIX Collaboration), Phys. Rev. Lett. **89**, 092302 (2002).
[43] J. Adams *et al.* (STAR Collaboration), Phys. Rev. Lett. **98**, 062301 (2007).

[44] R. E. Ansorge *et al.* (UA5 Collaboration), Nucl. Phys. B **328**, 36 (1989).
[45] B. Hippolyte (STAR Collaboration), arXiv:nucl-ex/0306017.
[46] A. E. M. Billmeier (STAR Collaboration), J. Phys. G **30**, S363 (2004).
[47] See Supplemental Material at http://link.aps.org/supplemental/10.1103/PhysRevC.88.024906 for tabulated values of results plotted in Figs. 4, 11, and 12.
[48] A. Adare *et al.* (PHENIX Collaboration), Phys. Rev. C **83**, 064903 (2011).
[49] G. Agakishiev *et al.* (STAR Collaboration), Phys. Rev. Lett. **108**, 072302 (2012).
[50] X.-N. Wang, Phys. Rev. C **58**, 2321 (1998).
[51] M. Kaneta and N. Xu, J. Phys. G: Nucl. Part. Phys. **30**, S1217 (2004).
[52] J. Cleymans, B. Kampfer, M. Kaneta, S. Wheaton, and N. Xu, Phys. Rev. C **71**, 054901 (2005).
[53] A. Adare *et al.* (PHENIX Collaboration), Phys. Rev. C **83**, 024909 (2011).
[54] R. C. Hwa and C. B. Yang, Phys. Rev. C **75**, 054904 (2007).
[55] A. Adare *et al.* (PHENIX Collaboration), Phys. Rev. Lett. **101**, 232301 (2008).
[56] S. S. Adler *et al.* (PHENIX Collaboration), Phys. Rev. Lett. **98**, 172302 (2007).
[57] B. I. Abelev *et al.* (STAR Collaboration), Phys. Rev. Lett. **97**, 152301 (2006).
[58] S. S. Adler *et al.* (PHENIX Collaboration), Phys. Rev. C **76**, 034904 (2007).
[59] S. S. Adler *et al.* (PHENIX Collaboration), Phys. Rev Lett. **91**, 072303 (2003).
[60] B. B. Back *et al.* (PHOBOS Collaboration), Phys. Rev. Lett. **93**, 082301 (2004).
[61] K. J. Eskola, H. Paukkunen, and C. A. Salgado, J. High Energy Phys. 04 (2009) 065.